

SPECTRAL AND TIMING EVOLUTION OF THE BLACK HOLE X-RAY NOVA 4U 1543–47 DURING ITS 2002 OUTBURST

S. Q. PARK¹, J. M. MILLER^{1,2}, J. E. MCCLINTOCK¹, R. A. REMILLARD³, J. A. OROSZ⁴, C. R. SHRADER⁵,
 R. W. HUNSTEAD⁶, D. CAMPBELL-WILSON⁶, C. H. ISHWARA-CHANDRA⁷, A. P. RAO⁷, M. P. RUPEN⁸

Draft version February 2, 2008

ABSTRACT

We present an X-ray spectral and timing analysis of 4U 1543–47 during its 2002 outburst based on 49 pointed observations obtained using the *Rossi X-ray Timing Explorer (RXTE)*. The outburst reached a peak intensity of 4.2 Crab in the 2–12 keV band and declined by a factor of 32 throughout the month-long observation. A 21.9 ± 0.6 mJy radio flare was detected at 1026.75 MHz two days before the X-ray maximum; the radio source was also detected late in the outburst, after the X-ray source entered the *hard* state. The X-ray light curve exhibits the classic shape of a rapid rise and an exponential decay. The spectrum is soft and dominated by emission from the accretion disk. The continuum is fit with a multicolor disk blackbody ($kT_{max} = 1.04$ keV) and a power-law ($\Gamma \sim 2.7$). Midway through the decay phase, a strong low-frequency QPO ($\nu = 7.3$ –8.1 Hz) was present for several days. The spectra feature a broad Fe K α line that is asymmetric, suggesting that the line is due to relativistic broadening rather than Comptonization. Relativistic Laor models provide much better fits to the line than non-relativistic Gaussian models, particularly near the beginning and end of our observations. The line fits yield estimates for the inner disk radius that are within $6 R_g$; this result and additional evidence indicates that this black hole may have a non-zero angular momentum.

Subject headings: accretion, accretion disks — binaries: close — black hole physics — stars: individual (IL Lupi, 4U 1543–47) — X-rays: stars

1. INTRODUCTION

The recurrent X-ray nova 4U 1543–47 was observed in outburst in 1971, 1983, 1992 and 2002 (Matilsky et al. 1972; Kitamoto et al. 1984; Harmon et al. 1992; this work). During the recent outburst, the peak X-ray intensity was 4.2 times that of the Crab Nebula (2–12 keV). The peak intensities during the three previous outbursts were comparable (Tanaka & Lewin 1995). The X-ray spectrum indicates that the primary is a black hole candidate: the 1–10 keV spectrum is invariably soft when the source is bright, and in 1992 a power-law component was observed with an intensity of ≈ 0.3 Crab in an energy band extending from 120 to 230 keV (Harmon et al. 1992; Tanaka & Lewin 1995).

The optical counterpart of 4U 1543–47, IL Lupi, was discovered by Pederson (1983). The secondary star has a relatively large mass and early spectral type, A2V (Chevalier & Ilovaisky 1992; McClintock & Remillard

2003). Because the secondary is relatively luminous, the optical counterpart brightens by only ≈ 1.8 mag in outburst (van Paradijs & McClintock 1995), although the X-ray source brightens by an enormous factor, $> 2 \times 10^7$ (Garcia et al. 2001), which is typical for an X-ray nova (McClintock & Remillard 2003). In the decade-long intervals of quiescence, the source intensity is $\lesssim 0.1 \mu\text{Crab}$. In this inert state, IL Lupi has been the subject of detailed dynamical studies by Orosz et al. (1998, 2003), who have derived the following primary data for this 26.8-hr binary: a black hole mass of $M_1 = 9.4 \pm 2.0 M_\odot$, a secondary star mass of $M_2 = 2.7 \pm 1.0 M_\odot$, and a distance of $D = 7.5 \pm 1.0$ kpc (where the distance error includes an uncertainty in the reddening of $E_{B-V} = 0.1$ mag). The large value of M_1 confirms that the compact primary is a black hole (Rhoades & Ruffini 1974). Of special importance for the present work, which focuses on the Fe K α line, 4U 1543–47 has a very low orbital inclination: $i = 20.7 \pm 1.0^\circ$ (Orosz et al. 2003).

During the 1983 outburst, a broad (FWHM ~ 2.7 keV) line centered at 5.9 keV was observed using the Gas Scintillation Proportional Counter (GSPC) aboard *EXOSAT* (van der Woerd, White & Kahn 1989). The higher resolution of the GSPC (relative to our study) makes this a pertinent result, which we return to in §4.2. Van der Woerd et al. interpreted this feature as a redshifted and broadened Fe K α line formed by Compton scattering and/or by Doppler and relativistic effects. More recently, a number of very *asymmetric* Fe K α line profiles with extended red wings have been observed in both Seyfert galaxies and black hole binaries (e.g., Tanaka & Lewin 1995; Miller et al. 2002). Relativistic beaming and gravitational redshifts in the inner disk region can serve to create such asymmetric profiles. Such broad Fe K α lines are thought to be generated by fluorescence through the

¹ Harvard-Smithsonian Center for Astrophysics, 60 Garden Street, Cambridge, MA 02138; spark@cfa.harvard.edu, jm-miller@cfa.harvard.edu, jem@cfa.harvard.edu

² NSF Astronomy and Astrophysics Fellow

³ Center for Space Research, MIT, Cambridge, MA 02139; rr@space.mit.edu

⁴ Department of Astronomy, San Diego State University, 5500 Campanile Drive, San Diego, CA 92182-1221; orosz@zwartgat.sdsu.edu

⁵ Laboratory for High-Energy Astrophysics, NASA Goddard Space Flight Center, Greenbelt, MD 20771; shrader@gssc.gsfc.nasa.gov

⁶ School of Physics, University of Sydney, NSW 2006, Australia; rwh@physics.usyd.edu.au, dcw@physics.usyd.edu.au

⁷ National Center for Radio Astrophysics, TIFR, Post Bag 3, Ganeshkhind, Pune 411 007, India; pramesh@ncra.tifr.res.in, ishwar@ncra.tifr.res.in

⁸ National Radio Astronomy Observatory, Socorro, NM 87801; mrupen@zia.aoc.nrao.edu

irradiation of the accretion disk by a source of hard X-rays, presumably a Comptonizing corona. (For recent reviews, see Fabian et al. 2000 and Reynolds & Nowak 2003.)

In the present work, we report on a 36-day campaign of 49 pointed observations made using the *Rossi X-ray Timing Explorer (RXTE)* Proportional Counter Array (PCA). We present the results of a spectral analysis that focuses on the behavior of the often intense, broad Fe $K\alpha$ line. We also present energy and power spectra for selected pointed observations. In §2 we discuss the observations and data reduction. The results of the spectral fitting are presented in §3, and a discussion of the Fe line and low frequency QPOs follows in §4. We conclude in §5 with a summary of our results.

2. OBSERVATIONS AND DATA REDUCTION

We observed 4U 1543–47 with *RXTE* on 49 occasions between Modified Julian Date (MJD = Julian Date – 2,400,000.5) 52442–52477 (2002 June 17 – 2002 July 22). These data correspond to all of the *RXTE* pointed observations made under programs 70133 and 70132, excluding a pair of observations made on 2002 July 1 that yielded problems with the archival data files. For four of the longest observations (Table 1: 0617, 0619, 0620, and 0628), we divided the exposures into two observing intervals. A list of the observation midpoint times and durations is given in Table 1. Owing to the extremely soft nature of this source, we did not include High Energy X-ray Timing Experiment (HEXTE) data in our analysis.

2.1. Spectroscopy

At the time of our data analyses, PCU–2 was the best-calibrated PCU in the *RXTE*/PCA (based on fits to observations of the Crab, which is taken to be a simple power-law in the *RXTE* band). As we wish to examine sometimes subtle Fe $K\alpha$ emission lines in the spectra of 4U 1543–47, we have therefore restricted our spectral analysis to include only data from PCU–2.

Data reduction tools from HEASOFT version 5.2 were used to screen the event files and spectra. Data were taken in the “Standard 2 mode”, which provides coverage of the full PCA bandpass (2–60 keV) every 16 seconds. Data from all Xe gas layers of PCU–2 were added to make the spectra. Background spectra were made using the tool “pcabackest” using the latest “bright source” background model. Background spectra were subtracted from the total spectra using the tool “mathpha”. Redistribution matrix files (rmfs) and ancillary response files (arfs) were generated for each PCU layer and combined into a single response file using the tool “pcarsp.”

It is well-known that fits to PCA spectra of the Crab nebula reveal residuals as large as 1%, and it has become customary to add systematic errors of 1% to all PCU energy channels (see, e.g., Sobczak et al. 2000). We therefore added systematic errors of 1% to all PCU–2 energy channels using the tool “grppha.” The spectral fits yielded no signs of residuals attributable to absorption from the Xe L3 edge at 4.79 keV (see, e.g., Miller et al. 2001; and Ibrahim, Swank, and Parke 2003), and therefore we did not include such an edge in our spectral model. Finally, strong deviations which cannot be accounted for by any plausible source spectral fea-

ture are found below 3 keV, and the spectrum becomes background-dominated and the calibration less certain above 25 keV. We therefore restricted our spectral analysis to the 2.9–25.0 keV band, which is customary for analysis of PCA spectra obtained after the gain change of 1999 March.

2.2. Timing

X-ray power density spectra (PDS) and the search for quasi-periodic oscillations (QPO) follow the descriptions given by Remillard et al. (2002). PDS in the frequency range 4 mHz to 4 kHz were computed for data in the energy range 2–30 keV for all of the observations listed in Table 1, with the exception of observations 10 and 11, where the data from fast PCA timing modes was not successfully telemetered. The data modes used for program 70133 provided opportunities to compute additional PDS to 4 kHz over any combination of energy bands: 2–6, 6–15, and 15–30 keV.

3. ANALYSIS AND RESULTS

The All Sky Monitor (ASM) total light curve from 2–12 keV and the ASM (5–12 keV)/(3–5 keV) hardness ratio (HR2) are plotted in Figure 1. The spectrum has a hardness ratio of ≈ 0.5 throughout most of the outburst, suggesting that the spectrum is soft (McClintock & Remillard 2003) and that thermal emission from an optically thick accretion disk is the dominant component of the spectrum (Shakura & Sunyaev 1973). The light curve exhibits the classic shape of a rapid rise and an exponential decay (Chen, Shrader, & Livio 1997; McClintock & Remillard 2003), with the source reaching a maximum intensity of 4.2 Crab at 2–12 keV near MJD 52445 (2002 June 20). The spectrum was initially hard during the rise to maximum. The source then transitioned to the *thermal dominant* (TD) state (McClintock & Remillard 2003), which is often referred to as the *high soft* state, where it remained for the next ~ 30 days. For several days during the decay phase, the source exhibited low-frequency QPOs and remained in the *steep power law* state (see §3.2), which is similar to the *intermediate* or *very high* state of black hole binaries. Finally, on MJD 52475 (2002 July 20) it entered the *hard* state at an intensity of ≈ 0.1 Crab. The ASM light curve can be compared with the PCA light curve in Figure 2, which is based on 49 pointed observations. The figure shows the total 2.9–25.0 keV unabsorbed flux over the observation period, along with the disk, power-law, and line components of the total flux.

All spectral analyses were performed using XSPEC version 11.2 (Arnaud 1996). Unless a source spectrum is strongly absorbed by the interstellar medium, the 2.9–25.0 keV band is not well-suited to measuring the equivalent neutral hydrogen column density. Attempts to determine this parameter via the 4U 1543–47 spectra using the “phabs” model consistently yielded error bars which included zero at 90% confidence. We therefore fixed this parameter to $N_H = 4.0 \times 10^{21} \text{ cm}^{-2}$ (Dickey & Lockman 1990, as implemented in the N_H tool on the HEASARC website). The transmission is 93% even at 2.9 keV, and therefore interstellar absorption is relatively unimportant.

In addition to interstellar absorption, the spectra were fit to a model that incorporates several other elements,

including a multicolor blackbody accretion disk component (Mitsuda et al. 1984; Makishima et al. 1986) and a power-law component. The fits returned the following continuum parameters: the color temperature at the inner edge of the disk in keV (T_{col}), the disk normalization parameter (K), the power-law photon index (Γ), and the power-law normalization factor. The disk normalization parameter K allows for the computation of an approximate inner disk radius (R_{col}):

$$K = \left(\frac{R_{col}/km}{D/10 \text{ kpc}} \right)^2 \cos i \quad (1)$$

where $D = 7.5$ kpc is the distance to the source and $i = 21^\circ$ is the inclination angle of the disk. Throughout this work we express the radius in units of the gravitational radius by dividing by $R_g \equiv GM/c^2$, where $M = 9.4 M_\odot$ is the black hole mass. Thus, for 4U 1543–47, $r_{col} = R_{col}/R_g = 0.056K^{1/2}$ (in units of R_g). We use the subscript “col” as a reminder that this estimate of the inner disk radius is based on a measurement of the apparent color temperature that is derived from a model that does not include effects of general relativity or electron scattering (see below). The values of the four continuum parameters over the course of the observations are summarized in Table 1 and plotted in Figure 3.

The thermal component of the emergent spectrum can be approximated as a diluted blackbody if electron scattering dominates over absorption as a source of opacity in the disk and if the X-ray spectrum is affected by Comptonization (Shakura & Sunyaev 1973; Ebisawa et al. 1994):

$$I(E) = \left(\frac{1}{f^4} \right) B(T_{col}, E), \quad (2)$$

where B is the Planck function and f is the spectral hardening factor. The values for T_{col} and r_{col} obtained from the fitting procedure systematically underestimate the actual disk radius, and the hardening factor f is generally needed to correct the results of the multicolor disk blackbody model, where the effective temperature and the effective radius are given by $T_{eff} = T_{col}/f$ and $r_{eff} = f^2 r_{col}$ (Shimura & Takahara 1995, see also Titarchuk & Shrader 2002). Merloni, Fabian, & Ross (2000) have presented two important results concerning corrections to the multicolor disk blackbody model. First, at low mass accretion rates and/or when a high fraction of the power is dissipated in the corona, simple correction factors do not allow physical disk parameters to be traced accurately. Second, when the mass accretion rate is high and/or a small fraction of the power is dissipated in the corona, the multicolor disk blackbody model gives results in which r_{col} underestimates the physical size of the inner disk by a constant factor (less than 2) over a broad range of conditions. A strong majority of the spectra we have obtained from 4U 1543–47 indicate that the second scenario holds, and we have therefore not applied a correction factor. We note that there are two periods where the power-law becomes relatively more important (in the middle of the campaign and at the end); however, for consistency we have not applied any correction to these spectral results. The source also has a very low inclination (21°), which further lessens the need for a hardening correction, since a low inclination angle generally implies a low optical depth to the source.

A broad smeared absorption edge (“smedge” in XSPEC) near 7.5 keV was included to approximately model the reflected continuum. Following Sobczak et al. (1999), we fixed the width at 7 keV, although we found that varying the width between 5–10 keV had little effect on our results. The returned parameters are the Fe edge energy in keV and the optical depth in the Fe line, τ (see Table 1).

The Fe $K\alpha$ feature was fit with a Laor model (Laor 1991), which assumes a Kerr black hole and accounts for relativistic effects, with the line energy fixed between 6.4 keV (neutral Fe) and 7 keV (H-like Fe). The following parameters of the Laor model were fixed: the power-law index of the radial dependence of emissivity at $q = 3$ (where $J \propto r^{-q}$), the outer radius at 400 gravitational radii, and the inclination angle at 21° . The fits to the Laor model returned values for line energy in keV, inner radius ρ in units of R_g , and line normalization factor in units of photons $\text{cm}^{-2} \text{s}^{-1}$. Figure 4 shows the evolution of ρ throughout our observation.

For comparison, the line was also fit with a Gaussian model (again with the line energy bounded between 6.4–7 keV). This line model returned parameters for line energy in keV, line width in keV, and line normalization in photons $\text{cm}^{-2} \text{s}^{-1}$. The fits to the Gaussian model yielded higher values of χ_ν^2 than fits to the Laor model, particularly near the beginning and end of the data set. Figure 5 shows the comparison between reduced chi-squared values for the Laor model and the Gaussian model for 40 degrees of freedom. Each of these models had a total of 9 free parameters (4 continuum, 2 smedge, and 3 line). The superiority of the fits obtained using the Laor model can be clearly illustrated by dividing our data into three sets. We find that the first 11 observations have a mean reduced chi squared value of 1.773 using the Gaussian model and 1.247 using the Laor model. The probabilities of exceeding these values of χ_ν^2 are $p = 0.0019$ and $p = 0.14$, respectively. The last 11 observations have a $\chi_\nu^2 = 1.496$ (Gaussian) and 0.917 (Laor), with $p = 0.23$ and 0.63, respectively. The middle 27 observations have mean χ_ν^2 of 0.904 (Gaussian) and 0.790 (Laor), with $p = 0.64$ and 0.83, respectively.

Figure 6 shows some sample spectra from the observations. The first pair of panels (a and b) show the ratio of the spectrum to the model for the observation with the worst fit, which occurred near the peak of the outburst. Panel (a) shows the observation after being fit with just the interstellar absorption, disk blackbody, and power-law components. Panel (b) shows the same observation after the Laor and smedge components have been included. The addition of these components reduces the χ_ν^2 drastically from 8.98 to 1.63. A more representative observation before and after the Laor and smedge components is shown in panels (c) and (d), respectively. The χ_ν^2 in this example decreased from 4.01 in panel (c) to 0.94 in panel (d).

Tables 1 and 2 list the returned values for all of the model parameters for fits to all 49 spectra. Unless otherwise noted, all errors reported in this work are at the 90% level of confidence.

3.1. Evolution of the Spectral Parameters

The color temperature of the inner disk increases through the first 7 observations, and then decreases

nearly monotonically during the rest of the observations (Fig. 3a). The color temperature is a factor of 2 lower in the final observations than in the initial observations. This trend in the color temperature closely traces the rise and fall of the disk flux (Fig. 2a & 3a). It is interesting to note that through the relatively smooth rise and long-term decline in color temperature, the implied inner disk radius remains rather steady (Fig. 3b). Indeed, the inner disk extent as measured by both the disk blackbody and Laor models does not appear to be correlated with the inner disk temperature or the disk flux during the phase of the outburst covered by our observations. However, r_{col} decreases near MJD 52460 when the power-law becomes strong. This is consistent with the idea stated above that simple correction factors do not allow physical disk parameters to be determined accurately when the power-law component is strong. It is important to note that the values of r_{col} are only approximate estimates, although the relative changes between the values are significant (see Section 4.3). We note that the 33% dip seen in the color radius during observations 18–20 (Table 1) may be primarily caused, in fact, by the simple effects of scattering losses as we view the disk through an enhanced corona that supplies the increased power-law flux during those same observations.

As the 2.9–25.0 keV emission is dominated by the disk, the total flux more closely traces the disk flux than the power-law flux. The power-law is strongest in the middle of our set of observations (MJD 52458–52464, approximately; Fig. 2c). During this time, and again toward the end of our set of observations (after MJD 52470), the fraction of the total flux contributed by the power-law exceeds 50%. Overall, the power-law index is remarkably steady (Fig. 3c). Moreover, the power-law index and normalization do not appear to be correlated on long timescales. However, on two occasions (near MJD 52444 and MJD 52471) the power-law normalization flared to higher values and on both occasions the power-law index softened considerably (see Fig. 3).

In Figure 7, we have plotted the power-law flux versus line flux and the disk component flux versus line flux. It is clear that both the disk and power-law fluxes are generally positively correlated with the line flux. The simplest picture of the accretion flow geometry around a Galactic black hole at a high mass accretion rate is that an accretion disk fuels a corona by the Compton-upscattering of disk photons. The corona in turn irradiates the disk and produces an Fe K α fluorescence emission line. The mass accretion rate through the disk should drive the disk, corona, and line flux on timescales comparable to the viscous timescale in the disk. The correlations shown in Figure 7b are broadly consistent with this simple picture. However, the measured relationship between the power-law flux and the line flux (Fig. 7a) unexpectedly deviates from a simple correlation, showing two branches with offset correlations between the two fluxes. The group with higher line emission relative to the power-law flux corresponds to observations 4–10 (see Table 2). These data were obtained during the interval of peak X-ray luminosity. It is conceivable that the increased line flux at such times is related to a higher ionization state near the surface of the disk, which would increase the strength of the line (Ross, Fabian & Young, 1999). This effect is not evident in Table 2; however,

the uncertainties are often as large as the expected line shift, and so the results are not conclusive. Alternatively, there may be correlations between the overall luminosity and the geometry of the power-law emitting region. In this case, the times of highest overall luminosity may be associated with a power-law emitting region that more efficiently illuminates the disk. This suggestion will be further discussed in Section 4.3.

3.2. Timing Results

The average PDS over four time intervals are shown in Figure 8. Within the indicated time intervals, the power spectra generally resemble the displayed average; furthermore, there are only modest changes in the X-ray spectral results within a given time interval (see Table 1). Observations that lie in the gaps between these time intervals (viz. MJD 52456–52458 and MJD 52474–52475) show characteristics of transition, and they are therefore excluded from the PDS averages.

The average PDS over MJD 52442–52455 shows a smooth power continuum that scales approximately as $P_\nu \propto \nu^{-1}$ (see Fig. 8a). During this time, as noted earlier, the disk displays a roughly constant color temperature and radius, while the unabsorbed flux from the disk (f_{disk}) exceeds that of the power-law component (f_{pow}). We find that throughout this time: $f_{disk}/(f_{disk} + f_{pow}) \gtrsim 0.7$, for fluxes integrated over the range of the PCA spectral fits (viz. 2.9–25.0 keV; see Fig. 2). The dominance of the disk is comparably evident if one chooses to integrate the flux over wider keV limits. For example, using the bolometric disk flux and the power-law flux at 1–25 keV, we find that the disk contributes more than 80% of the total flux (unabsorbed) throughout this time. These combined spectral and PDS characteristics are entirely consistent with the *thermal-dominant* (TD) state of black hole binaries (aka *high soft* state; McClintock & Remillard 2003).

A transition out of the TD state is seen during MJD 52456–52458, and weak QPOs appear in the PDS. On MJD 52457, a QPO is seen (6σ) centered at 10.1 Hz with an rms amplitude $r \sim 1.0\%$ and a coherence parameter $Q = \nu/\Delta\nu_{FWHM} \sim 8$. Similar results are seen on MJD 52458, with a QPO at $\nu = 10.0$ Hz, $r = 1.2\%$, and $Q \sim 5$. The QPO abruptly strengthens during MJD 52459–52461, and the average PDS is shown in Figure 8b. These three observations yield $\nu = 7.3$ –8.1 Hz, $r = 5.7$ –8.4%, and $Q \sim 6$ –9. The QPO profiles show obvious harmonic features on MJD 52459 and 52461, and these are also seen in the average PDS for this time interval. The bumps on either side of the strongest peak appear at frequencies 0.5ν and 2ν , as seen in other sources such as XTE J1550–564 (Remillard et al. 2002). During the interval of MJD 52459–52461, the spectral parameters shift toward smaller color radius and a stronger flux contribution from the power-law component: $f_{disk}/(f_{disk} + f_{pow}) \sim 0.45$ for 2.9–25.0 keV (or 0.7–0.8 if one uses the bolometric disk flux and the 1–25 keV power-law flux). The QPO detection, the increased strength of the power-law component, and the values of the photon index (2.5–2.7; see Table 1) are all consistent with the *steep power-law* (SPL) state of black hole binaries (McClintock & Remillard 2003).

After MJD 52461, the QPO abruptly disappears, as the PDS of MJD 52462 shows only a smooth continuum.

Meanwhile, the power-law flux rapidly decreases, and the disk color radius rebounds to values consistent with the MJD 52442–52455 results (Fig. 8a). These characteristics indicate a return to the TD state (Fig. 8c). The TD state continues with a gradually falling temperature, until MJD 52474, when the power-law spectrum and PDS continuum power both begin to build again. During the final days of our monitoring observations (MJD 52476–52477), a broad power peak is seen in the PDS near 2 Hz and a weak QPO returns at 9.7 Hz (see Fig. 8d). The photon index ($\Gamma = 2.4$) is lower at this time, and this trend continues in subsequent days, reaching $\Gamma = 1.7$ on MJD 52487, when the source has essentially completed its transition to the *hard* state (Kalemci et al. 2002; McClintock & Remillard 2003).

We searched for high-frequency QPOs (50–1000 Hz) in the PDS of each observation, in each available energy band. No significant detections were found. In the energy range 6–30 keV, the statistical upper limits (4σ) for a QPO at 200 Hz (assuming $Q \sim 5$) are $r < 0.9\%$ for the average PDS in the SPL state (MJD 52459–52461), and $r < 0.4\%$ for the TD state of MJD 52442–52455. At 800 Hz, again considering the average PDS shown in Fig. 8, the upper limits are only slightly lower at 0.7% for the SPL state and 0.3% for the TD state.

The X-ray light curves (1 s bins) for 4U 1543–47 always show the random flickering that is characteristic of black hole binaries. However, during the observation of 2002 July 6 (MJD 52461), which is the last day that the source was in the SPL state, there are hard dips suggestive of an accretion instability. This light curve is shown along with a PCA hardness ratio (HR) in Fig. 9. The dips generally last 5–10 s, the dip rate is roughly one per minute, and the dip minima have a constant value to within a few percent. We have also examined the spectral variations during the dips using a different HR quantity that selects 6–15 keV versus 2–6 keV. In this case there are almost no HR changes during the dips, despite the improved statistics. The latter result rules out the possibility that the dips are associated with photoelectric absorption due to intervening clouds.

The dips seen in 4U 1543–47 are reminiscent of some of the patterned variations seen in GRS 1915+105 (Belloni et al. 2000), which exhibits an amazing repertoire of unstable light curves. However, the dips in GRS 1915+105 with similar timescales (i.e. the γ and δ class variations) are spectrally “soft”, unlike those in 4U 1543–47. We further note that moderately unstable light curves have also been seen in GRO J1655–40 (Remillard et al. 1999), and dipping behavior has been seen on several occasions from 4U 1630–47 (Tomsick, Lapshov, & Kaaret 1998; Dieters et al. 2000).

3.3. Radio Observations and Results

Simultaneous radio observations were made during the X-ray outburst using two radio telescopes. The Molonglo Observatory Synthesis Telescope (MOST) observed the source at 843 MHz with a 3 MHz bandwidth in right-handed circular polarization; the synthesized beamwidth was $58'' \times 43''$ in position angle (PA) 0° . The Giant Metrewave Radio Telescope (GMRT), an aperture synthesis instrument consisting of thirty parabolic dishes each 45 m in diameter, observed the source in spectral line mode using a 16 MHz bandwidth. The GMRT observa-

tions were made at 1026.75 MHz (beamwidths $\sim 9'' \times 3''$), 1286.75 MHz ($6'' \times 2''$), and 616.75 MHz ($12'' \times 5''$), all with PA near 0° . The observations at 616.75 MHz were made using circularly polarized feeds, while the feeds at higher frequencies were linearly polarized; in all cases both independent polarizations were recorded. The errors given for the MOST detections represent the root-mean-square (rms) noise level measured near the source, while the errors for the GMRT detections are those given by the source fitting program. Systematic errors are $< 5\%$ for MOST but may be as high as 30% for GMRT due to the low elevation of the source. Upper limits on flux densities are three times the rms noise level measured in the vicinity of the source position.

A radio measurement made with MOST on MJD 52443.625 gave a position for 4U 1543–47 of $15^{\text{h}}47^{\text{m}}8^{\text{s}}.27$, $-47^\circ40'12''.8$ (J2000) with an error of $\sim 3''$. This is consistent with the positional measurements of the optical counterpart from the UK Schmidt images on the Super COSMOS website in the I-band: $15^{\text{h}}47^{\text{m}}8^{\text{s}}.32$, $-47^\circ40'10''.8$ (J2000) with errors of $\sim 0.25''$.

On MJD 52443, a 12-hour MOST survey observation detected a rapidly rising radio flare. During the first 6 hours (midpoint MJD 52443.375) the mean flux density was 6 ± 2 mJy, while the second 6 hours (MJD 52443.625) gave a mean of 16 ± 2 mJy, suggesting that the source had turned on quite suddenly. This was consistent with a 30-minute GMRT observation on the same day (MJD 52443.71) which gave a flux density of 21.9 ± 0.6 mJy at 1026.75 MHz. This radio flare occurred two days before the peak of the X-ray outburst and decayed quite rapidly. However, the appearance of the radio flare at the low frequencies of MOST and GMRT may be offset from the actual beginning of the flare if the radio outburst was initially optically thick at low frequencies. Observations of the source on the following day gave flux densities with upper limits of 2.7 mJy from a 12-hour observation with MOST (MJD 52444.50), and 2.1 mJy from a 20-minute observation with the GMRT (MJD 52444.71). The GMRT also detected a second radio flare with flux density 4.7 ± 0.3 mJy from a 2-hour observation on MJD 52445.71 at 1026.75 MHz and 5.3 ± 0.4 mJy from a 30-minute observation on MJD 52446.70 at 1286.75 MHz. The source went into a state of radio quiescence, with upper limits on the flux density of 3.0 mJy from the MOST data taken on MJD 52459.37 and 52480.40, 0.6 mJy from the GMRT on MJD 52447.70 (1286.75 MHz), and 3.2 mJy on MJD 52480.62 (616.75 MHz). Ten days after the X-ray observations reported here were completed and after the source had entered the *hard* state, the source was detected again at 5.2 ± 0.9 mJy in a 12-hour MOST observation on MJD 52487.38, but was quiescent on MJD 52496.33 with an upper limit of 2.4 mJy.

In a number of transient sources, the rising phase of an outburst is spectrally hard in X-rays and accompanied by a radio flare (for reviews, see Fender 2003, and McClintock & Remillard 2003). The initial radio detections of 4U 1543–47 are consistent with this picture. In the most extreme cases, a hard X-ray flare may be associated with blobs of material which are expelled at relativistic velocities, as seen in radio images (e.g., Hannikainen et al. 2000). The second radio flare seen here (MJD 52445–6) suggests a somewhat more complicated

situation, with further, on-going activity. Such additional flaring has been seen in a number of other sources, though on larger and longer scales; perhaps the best-observed analogue is GRO J1655–40 (Hjellming and Rupen 1995), where the re-flares were associated with multiple relativistic jet ejections, as well as substantial hard X-ray emission (Harmon et al. 1995). Unfortunately the radio observations discussed here do not have sufficient angular resolution to reveal extended emission from ejecta in 4U 1543–47.

The radio detection of 4U 1543–47 on MJD 52487 may either indicate another radio flare, or the transition to the *hard* state. The ratio of the power-law flux to the total flux (see Fig. 2) indicates a steep rise in the significance of the power-law spectral component starting on or near MJD 52474. The appearance of band limited noise in the power-density spectra and QPOs on MJDs 54476 and 52477 also signal a transition to the *hard* state (see Fig. 8). The situation is not quite so simple however, because (fainter) radio upper limits were derived on MJD 52480 and 52496, when the source also appeared to be in the same *hard* X-ray state.

4. DISCUSSION

4.1. Comparison with Earlier Outbursts of 4U 1543–47

It is problematic to compare the outbursts that occurred in 1971, 1983, 1992 and 2002 because of the differences in both instrumentation and observing coverage (Tanaka & Lewin 1995; Chen et al. 1997). Nevertheless, we make a few comparisons, after setting aside the 1992 outburst, which was quite shortlived and observed only above 20 keV (Harmon et al. 1992). For the three remaining outbursts, the spectra were very soft when the source was bright, and the peak X-ray intensities were 1.9 Crab (2–6 keV) in 1971, 4.0 Crab (3.7–7.5 keV) in 1983, and 3.3 Crab (3.7–7.5 keV) on 20 June 2002 (Matilsky et al. 1972; Kitamoto et al. 1984; this work). During the bright outburst in 1983, the luminosity above 1.5 keV was $2.5 \pm 0.3 \times 10^{39}$ erg s^{−1} for $D = 7.5$ kpc (Kitamoto et al. 1984), which nominally exceeds the Eddington luminosity of a 9.4 M_⊙ black hole by a factor of 2.1. As indicated above, the peak luminosity during the 2002 outburst was within about 85% of the overall maximum luminosity reached in 1983. However, the intensity in 2002 dropped rapidly with a decay time (1/e) of ≈ 13 days (see Fig. 1). By comparison, the peak intensity decayed 4–5 times more slowly in 1971.

4.2. Fe K α Emission Line Diagnostics

Iron line features are likely produced when hard X-rays created in a hot corona around a black hole irradiate a cold accretion disk and generate a fluorescent Fe line (see, e.g., Shapiro & Teukolsky 1983). This emission line serves as a diagnostic for studies of gravitation near the black hole. The defining property of a black hole is its event horizon, a surface through which particles and photons can fall inward, but through which nothing can pass outward. For a non-rotating Schwarzschild black hole, the radius of the event horizon is $R_S = 2(GM/c^2) \equiv 2 R_g$ and the innermost stable circular orbit is $R_{ISCO} = 6 R_g$. For a maximally-rotating Kerr black hole, $R_K = R_{ISCO} \approx 1 R_g$. Line emissions allow us to probe the inner-disk accretion region and distinguish between static and rotating black holes.

At its creation, a fluorescent Fe line is narrow and centered between 6.4 keV for neutral iron and 7 keV for hydrogenic iron. However, the observed line is severely broadened. One broadening mechanism that has been much discussed is Comptonization. Model calculations show that a line can be broadened due to Compton down-scattering in an optically-thick cloud that is highly ionized (Czerny, Zbyszewska, Raine 1991; see also Fabian et al. 1995). In this scenario, an Fe K α fluorescent line in an accretion disk could be broadened by multiple Compton scatterings in an optically-thick corona. This model predicts a broad, *symmetric* line profile and a break in the power-law continuum near 40 keV. Numerous scatterings are required to downshift an Fe K α photon by the 1 keV or more that is frequently observed (e.g., Miller et al. 2002). For example, even in the extreme case of a 180° backscattering event, an Fe K α photon loses only $\lesssim 0.2$ keV.

The Fe line can also be broadened due to relativistic distortions if it is emitted from an accretion disk that is close to the black hole (for reviews see Fabian et al. 2000; Reynolds & Nowak 2003). In the models, relativistic beaming boosts the blue wing of the line while attenuating the red wing, and gravitational redshifts displace the profile down to lower energies. The resultant profile is broad and *asymmetric*, with its exact shape being a function of geometrical parameters in the emitting regions, such as disk inner and outer radii, and inclination angle.

The strongest emission lines we have observed demonstrate a very asymmetric profile (a representative example is shown in Fig. 6a), which argues against Comptonization as the broadening mechanism. Furthermore, the small inclination angle of the source ($i = 21^\circ$) downplays the importance of Comptonization, in an effect discussed by Petrucci et al. (2001). These authors conclude that decreasing the inclination angle has the same effect as decreasing the optical depth, thereby decreasing the probability of a photon being Comptonized. The Laor model, which assumes a Kerr black hole and accounts for strong Doppler shifts and gravitational redshifts, naturally predicts an asymmetric profile that is similar to the one we observe. Indeed, the Laor model provides a good fit to all of our Fe line data, including those intractable profiles for which the Gaussian model fails (Fig. 5). Thus, we conclude that the Fe line is broadened largely by relativistic effects occurring in an accretion disk.

Results from both the continuum and line fits suggest that the inner edge of the accretion disk may extend within $6R_g$ (see Tables 1 & 2, and Figures 3b and 4), which may serve as an indication for a non-zero spin parameter. To better assess the possibility of black hole spin in 4U 1543–47, we examined the broad Fe line profile observed in 1983 with the superior resolution of the EXOSAT/GSPC (see §1). We chose to fit this spectrum with the same models herein applied to our RXTE observations, rather than the Comptonization model fitted previously by the authors. As with many of our spectra, the Gaussian model fails to fit the data, and a Laor line model is required (although a smeared edge is not). To enable a direct comparison to both our profiles (e.g., Fig. 6) and the profile featured by van der Woerd et al. (1989), we show in Figure 10 both the fit residuals and the ratio data/model. The residuals are remarkably similar to

those obtained by van der Woerd et al. using the Comptonization model, which indicates that the line profile is largely *independent* of the particular continuum model. Moreover, the line profile appears to be double-peaked, consistent with the best-studied lines in AGN. Fitting the *EXOSAT* spectrum with the Laor model suggests a line of only moderate strength ($EW = 180 \pm 60$ eV), but from a high charge state ($E = 6.87 - 7$ keV) compared to the *RXTE* results summarized in Table 2. Significantly, the *EXOSAT* Fe K α line more strongly requires emission from within $6 R_g$: $\rho = 3.3 \pm 0.6$ in units of R_g .

Van der Woerd et al. (1989) fit the Fe line with a Gaussian and found the central energy of the line to be 5.93 ± 0.24 keV. We also find that the line center shifts downward to a mean value of ≈ 5.4 keV when we fit the *RXTE* line profiles allowing the Gaussian to float down to a lower energy limit of 5 keV. These fits provided reduced chi-squared values similar to the ones obtained by fitting a Laor model. However, as we noted earlier, because the Fe lines we observed are obviously asymmetric (e.g., Fig. 6a), we favor the more physical Laor model to an unbounded Gaussian model. This choice is further supported by the Fe line profiles observed for other sources at higher resolution, which show that the lines are generally asymmetric, as well as by theoretical considerations which favor relativistic asymmetric broadening.

It should be noted that this analysis marks the first published attempt to systematically fit numerous Galactic black hole X-ray spectra with a relativistic emission line model, while covering a range in luminosity with variations by a factor > 30 during a single outburst. The brightness and low inclination of 4U 1543–47 presents a special opportunity to study the source in greater detail. Laor models clearly have the potential to provide important constraints on the inner accretion flow and the nature of the black hole itself. Prior efforts to fit numerous spectra spanning transient black hole outbursts have primarily relied on Gaussian models, and may have missed valuable information.

4.3. Constraining the Accretion Flow Geometry

The disk blackbody model parameters summarized in Table 1 indicate that the inner disk edge likely remained relatively stable within the marginally stable circular orbit of a black hole despite a decline in total flux by a factor of 32 and a drop in the color temperature of the inner disk by a factor of 2. This constancy of r_{col} over a wide range of mass accretion rates has been observed for a number of X-ray novae during their decline (e.g., Tanaka & Lewin 1995; Sobczak et al. 2000). When the power-law flux is low or moderate, we regard the values of r_{col} in Table 1 as a good indicator of relative changes in the inner disk, as well as an approximate indicator of the inner disk radius. However, these values do not include relativistic corrections (e.g., Zhang, Cui & Chen 1997) or corrections for the effects of electron scattering (§3), which are themselves quite uncertain (Merloni et al. 2000). Also, the errors in r_{col} in Table 1, have not been calculated to include errors in the distance, the mass of the black hole, and the binary inclination. The former two uncertainties (see §1) are dominant and translate into an error of 25% on r_{col} . Not only was r_{col} fairly stable during all of our observations, the values of ρ inferred from the Laor model were similarly stable throughout

(Table 2, Fig. 4).

The fact that the power-law and Fe K α line fluxes are correlated on long time scales (Fig. 2cd) confirms the basic disk reflection picture described by George & Fabian (1991) and the models developed by Zdziarski et al. (2003). The line flux peaks at the start of the outburst, during the same observations when the disk color temperature is highest. However, during this early phase the power-law flux is not at its absolute peak value; moreover, it reaches a much higher fraction of the total flux at later phases of the outburst (Fig. 2e). Assuming that the hard X-ray emission arises in an optically thin corona, the early maximum in the Fe K α line (despite the modest level of the power-law flux) may indicate that the corona was more centrally-concentrated and/or it illuminated the disk more centrally early in the outburst. A similar suggestion was made to explain differences in the Fe K α emission line profile in the Seyfert-1 galaxy MCG-6-30-15 (Iwasawa et al. 1996).

As noted previously, the binary inclination of 4U 1543–47 is very low, $i = 21^\circ$. If we assume that the inner disk is seen at a similar inclination (a reasonable assumption given the success of fits with the Laor model which assume this inclination), then the axis of any jet outflow may be close to our line of sight. Recently, it has been suggested that the hard X-ray component in Galactic black holes may due to direct synchrotron emission and/or synchrotron self-Comptonization in the jet (Markoff, Falcke, & Fender 2001; Markoff et al. 2003). It is therefore particularly interesting to assess the role of a jet in 4U 1543–47.

Some aspects of our results argue against associating the hard X-ray emission in 4U 1543–47 with a jet, at least in this phase of the outburst. First, the power-law index is rather soft; synchrotron radiation from a jet with a flat to “inverted” radio spectrum should be spectrally harder. Also, the Lorentz factors required to generate X-ray synchrotron emission in a jet would beam the hard X-ray emission in a narrow cone along the jet axis and away from the disk. This is inconsistent with our observation of a broad and intense Fe K α emission line which is very likely produced by hard X-ray emission shining “down” onto the accretion disk. For example, the X-ray reflection models of George & Fabian (1991) predict an Fe K α equivalent width of $\lesssim 120$ eV for $i = 21^\circ$ and the steep power-law indices observed by us ($\Gamma > 2.3$; see their Fig. 14). Averaged over all of our observations, the equivalent width of the Fe K α line is ≈ 2 times this predicted value, and it is occasionally 3–4 times greater (Table 2). Clearly, the large line equivalent widths we measure demand that a high fraction of the total hard flux be intercepted by the disk, which is incompatible with the emission being beamed away from the disk.

5. SUMMARY AND CONCLUSIONS

We have analyzed the spectral and timing properties 4U 1543–47 during the bright phase of its 2002 outburst using observations obtained with the *RXTE*/PCA. The outburst, which exhibited a fast rise and an exponential decay, was dominated throughout our observations by soft thermal emission from the accretion disk; the source was generally in the *thermal dominant* state. However, midway through the decay phase, the source entered the *steep power-law* state and strong low-frequency QPOs

were detected with obvious harmonic features. As frequently observed for this state, the power-law flux increased to a maximum and the radius of the inner disk inferred from the color temperature, r_{col} , decreased. Near the end of our observations, a low-frequency QPO reappeared and the power-law spectrum hardened as the source entered the *hard* state.

A radio flare was detected near the peak of the X-ray outburst by MOST and GMRT with a peak flux density of 21.9 ± 0.6 mJy. Smaller flares were also detected just after the X-ray peak, as well as after the source entered the *hard* state. The radio observations did not have sufficient angular resolution to reveal evidence of extended emission from ejected blobs.

The most striking feature of the X-ray spectrum is a broad, asymmetric Fe K α emission line. We fit this line in each of our spectra using the Laor relativistic line model, which generally provided a much better fit to our data than Gaussian models. Despite the low resolution of the *RXTE*/PCA, about half the spectral fits suggest that 4U 1543–47 contains a black hole with non-zero angular momentum. The higher resolution *EXOSAT* spectrum (Van der Woerd et al. 1989) lends further, significant support to the suggestion that 4U 1543–47 contains a Kerr black hole.

Although numerous transient black hole outbursts have been observed extensively with the *RXTE*/PCA and prior observatories such as *Ginga*, this is the first systematic effort to fit a relativistic line model to numerous spectra which span an order of magnitude in flux. Our results suggest that proportional counter data obtained in earlier synoptic studies of black hole binaries can be reanalyzed using a relativistic emission line model to obtain important constraints on the nature of the black hole and the geometry of the accretion flow.

This work is supported in part by NASA Grant NAG5–10813. This work has made use of the information and tools available at the HEASARC website, operated by GSFC for NASA. We thank the staff of GMRT that made these observations possible. GMRT is run by the National Centre of Radio Astrophysics of the Tata Institute of Fundamental Research. MOST is operated by the University of Sydney and supported in part by grants from the Australian Research Council.

REFERENCES

- Arnaud, K. A. 1996, in ASP Conf. Ser. 101: Astronomical Data Analysis Software and Systems V., 17
- Belloni, T., Klein-Wolt, M., Mendez, M., van der Klis, M., & van Paradijs, J. 2000, A&A, 355, 271
- Chen, W., Shrader, C. R., & Livio, M. 1997, ApJ, 491, 312
- Chevalier, C., Ilovaisky, S. A. 1992, IAU Circ., 5520, 1
- Czerny, B., Zbyszewska, M., & Raine, D. J. 1991, in Proc. Iron Line Diagnostics in X-ray Sources (Varenna 1990), ed. A. Treves, G. C. Perola, & L. Stella, Lecture Notes in Physics (Berlin: Springer-Verlag), vol. 385, 226
- Dickey, J. M. & Lockman, F. J. 1990, ARA&A, 28, 215
- Dieters, S. W., et al. 2000, ApJ, 538, 307
- Ebisawa, K., et al. 1994, PASJ, 46, 375
- Fabian, A. C., Iwasawa, K., Reynolds, C. S. & Young, A. J. 2000, PASP, 112, 1145
- Fabian, A. C., Nandra, K., Reynolds, C. S., Brandt, W. N., Otani, C., Tanaka, Y., Inoue, H., & Iwasawa, K. 1995, MNRAS, 277, L11
- Fender, R. P., 2003, to appear in "Compact Stellar X-ray Sources", eds. W. H. G. Lewin and M. van der Klis, Cambridge: Cambridge University Press
- Garcia, M. R., McClintock, J. E., Narayan, R., Callanan, P., Barret, D., & Murray, S. S. 2001, ApJ, 553, L47
- George, I. M. & Fabian, A. C. 1991, MNRAS, 249, 352
- Hannikainen, D., et al., 2000, ApSSS, 276, 45
- Hannikainen, D. C., Hunstead, R. W., Campbell-Wilson, D., Wu, K., McKay, D. J., Smits, D. P., & Sault, R. J. 2000 ApJ, 540, 521
- Harmon, B. A., Wilson, R. B., Finger, M. H., Paciesas, W. S., Rubin, B. C., & Fishman, G. J. 1992, IAU Circ., 5504, 1
- Harmon, B. A., et al. 1995, Nature, 374, 703
- Hjellming, R. M., & Rupen, M. P. 1995, Nature, 375, 464
- Ibrahim, A. I., Swank, J. H., & Parke, W. 2003, ApJ, 584, L17
- Iwasawa, K., et al. 1996, MNRAS, 282, 1038
- Kalemci, E., Tomsick, J., Rothschild, R., Corbel, S., Kaaret, P., & McClintock, J. 2002, ATEL, 103
- Kitamoto, S., Miyamoto, S., Tsunemi, H., Makishima, K., & Nakagawa, M. 1984, PASJ, 36, 799
- Laor, A. 1991, ApJ, 376, 90
- Makishima, K., Maejima, Y., Mitsuda, K., Bradt, H. V., Remillard, R. A., Tuohy, I. R., Hoshi, R., & Nakagawa, M. 1986, ApJ, 308, 635
- Markoff, S., Falcke, H., & Fender, R. 2001, A&A, 372, L25
- Markoff, S., Nowak, M., Corbel, S., Fender, R., & Falcke, H. 2003, A&A, 397, 645
- Matilsky, T. A., Giacconi, R., Gursky, H., Kellogg, E. M., & Tananbaum, H. D. 1972, ApJ, 174, L53
- McClintock, J. E., & Remillard, R. A. 2003, to appear in Compact Stellar X-ray Sources, ed. W. H. G. Lewin & M. van der Klis, Cambridge: Cambridge Univ. Press, preprint (astro-ph/0306213)
- Merloni, A., Fabian, A. C., & Ross, R. R. 2000, MNRAS, 313, 193
- Miller, J. M., et al. 2002, ApJ, 578, 348
- Miller, J. M., Fox, D. W., Di Matteo, T., Wijnands, R., Belloni, T., Pooley, D., Kouveliotou, C., & Lewin, W. H. G. 2001, ApJ, 546, 1055
- Mitsuda, K., et al. 1984, PASJ, 36, 741
- Orosz, J. A. 2003, in preparation
- Orosz, J. A. and Jain, R. K., Bailyn, C. D., McClintock, J. E., & Remillard, R. A. 1998, ApJ, 499, 375
- Pedersen, H. 1983, The Messenger, 34, 21
- Petrucchi, P. O., Merloni, A., Fabian, A., Haardt, F., & Gallo, E. 2001, MNRAS, 328, 501
- Remillard, R. A., Morgan, E. H., McClintock, J. E., Bailyn, C. D., & Orosz, J. A. 1999, ApJ, 522, 397
- Remillard, R. A., Sobczak, G. J., Munro, M. P., & McClintock, J. E. 2002, ApJ, 564, 962
- Reynolds, C. S., & Nowak, M. A. 2003, Phys. Rept., 377, 389
- Rhoades, C. E., & Ruffini, R. 1974, Phys. Rev. Lett., 32, 324
- Ross, R. R., Fabian, A. C., Young, A. J. 1999, MNRAS, 306, 461
- Shakura, N. I., & Sunyaev, R. A. 1973, A&A, 24, 337
- Shapiro, S. L., & Teukolsky, S. A. 1983, Black Holes, White Dwarfs, and Neutron Stars: The Physics of Compact Objects (New York: Wiley)
- Shimura, T., & Takahara, F. 1995, ApJ, 445, 780
- Sobczak, G. J., McClintock, J. E., Remillard, R. A., Cui, W., Levine, A. M., Morgan, E. H., Orosz, J. A., & Bailyn, C. D. 2000, ApJ, 544, 993
- Tanaka, Y., & Lewin, W. H. G. 1995, X-ray Binaries, ed. W. H. G. Lewin, J. van Paradijs, & E. P. J. van den Heuvel (Cambridge: Cambridge Univ. Press)
- Titarchuk, L., & Shrader, C. R. 2002, ApJ, 567, 1057
- Thorne, K. S., 1974, ApJ, 191, 507
- Tomsick, J. A., Lapshov, I., & Kaaret, P. 1998, ApJ, 494, 747
- van der Woerd, H., White, N. E., & Kahn, S. M. 1989, ApJ, 344, 320
- van Paradijs, J., & McClintock, J. E. 1995, Optical and Ultraviolet Observations of X-ray Binaries, X-ray Binaries, eds. W.H.G. Lewin, J. van Paradijs, and E.P.J. van den Heuvel (Cambridge: Cambridge Univ. Press), 58
- Zdziarski, A. A., Lubiński, P., Gilfanov, M., & Revnivtsev, M. 2003, MNRAS, 342, 355
- Zhang, S. N., Cui, W., & Chen, W. 1997, ApJ, 482, L155

TABLE 1. PCA Data and Broadband Spectral Parameters for 4U 1543–47

Obs No.	Date (mmd)	MJD ^a	Obs. Time (s)	T_{col} ^b (keV)	r_{col} ^c (R_g)	Photon Index	Power-Law ^d Norm	Fe Edge ^e (keV)	τ_{Fe} ^e	Flux $\times 10^{-10}$ ^f (ergs cm ⁻² s ⁻¹)	χ^2_ν (40 dof)
1	0617	52442.83	2544	0.90 ^{+0.01} _{-0.02}	4.50 ^{+0.20} _{-0.21}	2.55 ^{+0.11} _{-0.09}	5.11 ^{+2.14} _{-1.31}	7.48 ^{+0.37} _{-0.38}	1.08 ^{+0.54} _{-0.48}	242.74 ^{+0.60} _{-1.61}	0.97
2	0617	52442.90	5216	0.91 ^{+0.02} _{-0.01}	4.45 ^{+0.18} _{-0.22}	2.52 ^{+0.10} _{-0.07}	5.06 ^{+1.85} _{-1.10}	7.55 ^{+0.33} _{-0.39}	1.10 ^{+0.51} _{-0.41}	257.69 ^{+0.61} _{-1.17}	0.87
3	0618	52443.26	2992	0.94 ^{+0.01} _{-0.01}	4.68 ^{+0.17} _{-0.17}	2.65 ^{+0.09} _{-0.08}	5.54 ^{+1.83} _{-1.18}	7.36 ^{+0.31} _{-0.26}	1.37 ^{+0.37} _{-0.37}	314.48 ^{+1.11} _{-1.28}	0.91
4	0619	52444.45	3552	1.02 ^{+0.01} _{-0.01}	4.49 ^{+0.09} _{-0.13}	3.71 ^{+0.21} _{-0.11}	33.69 ^{+27.47} _{-9.07}	7.63 ^{+0.19} _{-0.16}	1.63 ^{+0.31} _{-0.22}	453.91 ^{+1.01} _{-1.46}	1.63
5	0619	52444.52	3744	1.03 ^{+0.01} _{-0.01}	4.39 ^{+0.13} _{-0.13}	3.85 ^{+0.12} _{-0.12}	52.75 ^{+14.72} _{-14.72}	7.59 ^{+0.18} _{-0.18}	1.73 ^{+0.24} _{-0.24}	459.97 ^{+1.46} _{-2.10}	1.48
6	0620	52445.57	3968	1.02 ^{+0.01} _{-0.01}	4.61 ^{+0.15} _{-0.14}	2.93 ^{+0.09} _{-0.07}	16.52 ^{+5.44} _{-3.25}	7.76 ^{+0.31} _{-0.26}	1.20 ^{+0.32} _{-0.29}	501.46 ^{+1.29} _{-2.64}	1.30
7	0620	52445.64	4144	1.04 ^{+0.01} _{-0.01}	4.49 ^{+0.12} _{-0.14}	2.73 ^{+0.08} _{-0.06}	9.53 ^{+3.58} _{-0.80}	7.85 ^{+0.38} _{-0.30}	0.96 ^{+0.35} _{-0.25}	523.06 ^{+1.51} _{-2.36}	1.35
8	0621	52446.07	4432	1.04 ^{+0.01} _{-0.01}	4.70 ^{+0.13} _{-0.13}	3.41 ^{+0.16} _{-0.11}	19.26 ^{+5.86} _{-4.96}	7.65 ^{+0.18} _{-0.20}	1.41 ^{+0.28} _{-0.19}	491.25 ^{+1.24} _{-2.97}	1.41
9	0622	52447.00	4560	1.03 ^{+0.01} _{-0.01}	4.72 ^{+0.17} _{-0.16}	3.15 ^{+0.15} _{-0.09}	11.24 ^{+6.09} _{-2.91}	7.56 ^{+0.24} _{-0.27}	1.37 ^{+0.34} _{-0.26}	470.82 ^{+1.52} _{-1.36}	1.24
10	0623	52448.06	3312	1.02 ^{+0.01} _{-0.01}	4.45 ^{+0.18} _{-0.18}	2.91 ^{+0.09} _{-0.09}	6.446 ^{+1.47} _{-1.88}	7.59 ^{+0.22} _{-0.22}	1.35 ^{+0.28} _{-0.28}	438.86 ^{+1.49} _{-1.58}	1.42
11	0624	52449.11	2064	1.01 ^{+0.01} _{-0.01}	4.51 ^{+0.20} _{-0.16}	2.60 ^{+0.10} _{-0.09}	5.142 ^{+1.88} _{-1.25}	7.69 ^{+0.32} _{-0.29}	1.19 ^{+0.33} _{-0.32}	420.92 ^{+1.58} _{-1.60}	1.14
12	0625	52450.25	1680	0.97 ^{+0.01} _{-0.01}	4.52 ^{+0.19} _{-0.20}	2.68 ^{+0.10} _{-0.08}	6.18 ^{+1.93} _{-1.39}	7.44 ^{+0.28} _{-0.14}	1.29 ^{+0.32} _{-0.30}	375.10 ^{+1.56} _{-1.81}	0.75
13	0626	52451.57	1856	0.95 ^{+0.01} _{-0.01}	4.50 ^{+0.22} _{-0.19}	2.75 ^{+0.10} _{-0.09}	6.76 ^{+2.22} _{-1.69}	7.29 ^{+0.26} _{-0.19}	1.63 ^{+0.35} _{-0.41}	333.55 ^{+0.98} _{-1.54}	0.79
14	0627	52452.69	2496	0.97 ^{+0.01} _{-0.01}	4.63 ^{+0.19} _{-0.20}	2.48 ^{+0.05} _{-0.08}	3.34 ^{+1.04} _{-0.69}	7.38 ^{+0.29} _{-0.39}	1.44 ^{+0.32} _{-0.34}	329.47 ^{+1.18} _{-1.06}	0.69
15	0628	52453.50	1344	0.93 ^{+0.01} _{-0.02}	4.60 ^{+0.20} _{-0.17}	2.55 ^{+0.10} _{-0.08}	7.99 ^{+2.93} _{-1.85}	7.99 ^{+0.36} _{-0.38}	0.82 ^{+0.39} _{-0.39}	314.14 ^{+1.43} _{-1.43}	0.71
16	0628	52453.55	3584	0.93 ^{+0.01} _{-0.02}	3.90 ^{+0.20} _{-0.17}	2.59 ^{+0.10} _{-0.08}	7.57 ^{+2.96} _{-1.67}	7.64 ^{+0.37} _{-0.40}	0.95 ^{+0.52} _{-0.50}	306.95 ^{+0.99} _{-1.26}	0.60
17	0629	52454.60	2048	0.91 ^{+0.01} _{-0.02}	3.88 ^{+0.19} _{-0.19}	2.57 ^{+0.12} _{-0.08}	7.06 ^{+3.46} _{-1.56}	7.65 ^{+0.33} _{-0.35}	1.07 ^{+0.63} _{-0.40}	280.12 ^{+0.86} _{-1.62}	0.63
18	0630	52455.13	656	0.91 ^{+0.01} _{-0.02}	3.34 ^{+0.22} _{-0.25}	2.41 ^{+0.21} _{-0.14}	2.73 ^{+2.58} _{-0.96}	7.41 ^{+1.89} _{-0.31}	0.52 ^{+0.95} _{-0.52}	253.72 ^{+0.88} _{-1.30}	0.95
19	0701	52456.77	4944	0.88 ^{+0.01} _{-0.02}	3.41 ^{+0.27} _{-0.25}	2.46 ^{+0.12} _{-0.12}	3.08 ^{+1.49} _{-0.76}	7.57 ^{+0.43} _{-0.39}	0.90 ^{+0.63} _{-0.47}	215.46 ^{+0.95} _{-1.39}	0.57
20	0702	52457.83	1776	0.90 ^{+0.02} _{-0.02}	3.27 ^{+0.23} _{-0.21}	2.74 ^{+0.07} _{-0.11}	10.62 ^{+2.14} _{-2.14}	7.85 ^{+0.36} _{-0.36}	1.15 ^{+0.36} _{-0.36}	222.76 ^{+1.10} _{-1.10}	0.97
21	0703	52458.44	1904	0.89 ^{+0.02} _{-0.02}	3.72 ^{+0.22} _{-0.19}	2.77 ^{+0.11} _{-0.09}	11.55 ^{+4.68} _{-2.78}	7.70 ^{+0.30} _{-0.43}	1.32 ^{+0.57} _{-0.46}	210.91 ^{+0.64} _{-0.81}	0.85
22	0704	52459.08	1152	0.90 ^{+0.02} _{-0.03}	3.78 ^{+0.22} _{-0.18}	2.72 ^{+0.11} _{-0.07}	16.05 ^{+6.39} _{-3.39}	7.67 ^{+0.31} _{-0.37}	1.30 ^{+0.62} _{-0.41}	227.65 ^{+0.47} _{-1.04}	0.69
23	0705	52460.49	1216	0.87 ^{+0.02} _{-0.03}	4.52 ^{+0.29} _{-0.16}	2.51 ^{+0.10} _{-0.05}	9.03 ^{+3.32} _{-1.45}	7.94 ^{+0.32} _{-0.41}	1.13 ^{+0.59} _{-0.30}	196.09 ^{+0.53} _{-0.85}	0.66
24	0706	52461.41	880	0.86 ^{+0.03} _{-0.03}	4.80 ^{+0.23} _{-0.22}	2.64 ^{+0.10} _{-0.08}	11.61 ^{+4.48} _{-2.70}	7.70 ^{+0.39} _{-0.35}	1.40 ^{+0.59} _{-0.45}	180.08 ^{+0.37} _{-0.32}	0.92
25	0707	52462.57	4928	0.83 ^{+0.02} _{-0.02}	4.58 ^{+0.19} _{-0.19}	2.59 ^{+0.06} _{-0.06}	5.47 ^{+1.46} _{-1.01}	7.89 ^{+0.35} _{-0.24}	1.53 ^{+0.36} _{-0.36}	130.59 ^{+0.54} _{-0.54}	0.94
26	0708	52463.67	4816	0.81 ^{+0.02} _{-0.02}	4.68 ^{+0.36} _{-0.30}	2.61 ^{+0.09} _{-0.06}	4.05 ^{+1.26} _{-0.73}	7.99 ^{+0.24} _{-0.27}	1.55 ^{+0.47} _{-0.34}	107.84 ^{+0.39} _{-0.46}	0.71
27	0709	52464.45	2768	0.76 ^{+0.01} _{-0.02}	4.58 ^{+0.23} _{-0.18}	2.32 ^{+0.24} _{-0.11}	0.61 ^{+0.68} _{-0.17}	7.95 ^{+0.51} _{-0.56}	1.23 ^{+1.22} _{-0.51}	75.087 ^{+0.17} _{-0.45}	0.73
28	0710	52465.08	1200	0.73 ^{+0.01} _{-0.01}	4.84 ^{+0.30} _{-0.22}	2.40 ^{+0.24} _{-0.15}	0.75 ^{+0.82} _{-0.26}	7.94 ^{+0.61} _{-0.59}	1.56 ^{+1.19} _{-0.67}	69.27 ^{+0.51} _{-0.24}	0.82
29	0711	52466.34	2720	0.72 ^{+0.01} _{-0.02}	4.77 ^{+0.25} _{-0.32}	2.35 ^{+0.10} _{-0.09}	0.79 ^{+0.28} _{-0.17}	8.08 ^{+0.31} _{-0.39}	1.82 ^{+0.47} _{-0.39}	59.62 ^{+0.20} _{-0.35}	0.99
30	0712	52467.20	1888	0.70 ^{+0.02} _{-0.02}	5.04 ^{+0.23} _{-0.23}	2.62 ^{+0.25} _{-0.12}	1.35 ^{+0.72} _{-0.35}	7.43 ^{+0.33} _{-0.45}	2.06 ^{+1.20} _{-1.12}	51.91 ^{+0.35} _{-0.14}	0.87
31	0713	52468.66	3328	0.69 ^{+0.01} _{-0.01}	5.00 ^{+0.42} _{-0.24}	2.31 ^{+0.12} _{-0.14}	0.34 ^{+0.35} _{-0.11}	8.01 ^{+0.55} _{-0.55}	2.08 ^{+0.57} _{-0.57}	41.03 ^{+0.19} _{-0.19}	0.61
32	0713	52468.73	1648	0.68 ^{+0.01} _{-0.01}	4.99 ^{+0.19} _{-0.26}	2.58 ^{+0.23} _{-0.20}	0.68 ^{+0.56} _{-0.30}	7.63 ^{+0.42} _{-0.43}	3.13 ^{+0.84} _{-0.92}	39.84 ^{+0.17} _{-0.26}	0.87
33	0714	52469.24	1760	0.67 ^{+0.01} _{-0.01}	4.76 ^{+0.29} _{-0.33}	2.47 ^{+0.25} _{-0.16}	0.47 ^{+0.45} _{-0.15}	8.04 ^{+0.48} _{-0.63}	1.85 ^{+0.94} _{-0.57}	37.64 ^{+0.20} _{-0.26}	0.71
34	0714	52469.31	3104	0.65 ^{+0.01} _{-0.01}	5.22 ^{+0.34} _{-0.30}	2.47 ^{+0.20} _{-0.14}	0.57 ^{+0.44} _{-0.19}	7.66 ^{+0.35} _{-0.40}	2.78 ^{+0.95} _{-0.66}	35.64 ^{+0.17} _{-0.20}	0.82
35	0715	52470.24	1376	0.65 ^{+0.01} _{-0.02}	5.26 ^{+0.30} _{-0.30}	2.52 ^{+0.01} _{-0.01}	0.55 ^{+0.24} _{-0.24}	7.49 ^{+0.39} _{-0.39}	3.21 ^{+1.04} _{-1.04}	31.78 ^{+0.22} _{-0.22}	0.89
36	0715	52470.30	3472	0.64 ^{+0.01} _{-0.01}	5.13 ^{+0.35} _{-0.36}	2.66 ^{+0.12} _{-0.15}	0.85 ^{+0.33} _{-0.32}	7.27 ^{+0.27} _{-0.17}	3.75 ^{+0.47} _{-0.92}	31.87 ^{+0.16} _{-0.21}	0.65
37	0715	52470.98	592	0.62 ^{+0.01} _{-0.01}	5.19 ^{+0.24} _{-0.31}	3.84 ^{+0.19} _{-0.22}	5.57 ^{+3.61} _{-3.40}	7.18 ^{+0.81} _{-0.08}	1.69 ^{+1.25} _{-1.45}	24.09 ^{+0.02} _{-0.68}	0.99
38	0716	52471.02	1072	0.62 ^{+0.01} _{-0.01}	5.19 ^{+0.31} _{-0.34}	3.09 ^{+0.28} _{-0.27}	1.44 ^{+1.46} _{-0.80}	7.17 ^{+0.41} _{-0.07}	4.04 ^{+1.33} _{-1.74}	26.56 ^{+0.07} _{-0.31}	0.93
39	0717	52472.62	2048	0.59 ^{+0.01} _{-0.02}	4.77 ^{+0.49} _{-0.51}	2.75 ^{+0.21} _{-0.18}	0.76 ^{+0.32} _{-0.42}	7.25 ^{+0.46} _{-0.13}	2.89 ^{+0.65} _{-0.85}	20.58 ^{+0.12} _{-0.29}	0.63
40	0717	52472.69	1712	0.60 ^{+0.01} _{-0.01}	4.25 ^{+0.20} _{-0.20}	2.54 ^{+0.21} _{-0.21}	0.53 ^{+0.23} _{-0.23}	7.45 ^{+0.35} _{-0.35}	3.38 ^{+0.94} _{-0.94}	20.88 ^{+0.18} _{-0.18}	1.11
41	0718	52473.20	1760	0.59 ^{+0.01} _{-0.00}	4.65 ^{+0.52} _{-0.98}	2.67 ^{+0.08} _{-0.10}	0.93 ^{+0.19} _{-0.23}	7.10 ^{+0.27} _{-0.00}	2.71 ^{+0.30} _{-0.79}	21.02 ^{+0.08} _{-0.14}	0.84
42	0718	52473.27	2864	0.59 ^{+0.01} _{-0.01}	4.39 ^{+0.68} _{-0.64}	2.60 ^{+0.12} _{-0.13}	0.72 ^{+0.25} _{-0.22}	7.26 ^{+0.33} _{-0.16}	3.09 ^{+0.49} _{-0.70}	20.47 ^{+0.08} _{-0.16}	0.87
43	0719	52474.18	1104	0.58 ^{+0.02} _{-0.02}	4.45 ^{+0.10} _{-0.13}	2.56 ^{+0.13} _{-0.14}	1.02 ^{+0.39} _{-0.32}	7.32 ^{+0.44} _{-0.22}	2.75 ^{+0.49} _{-0.66}	20.35 ^{+0.12} _{-0.28}	0.86
44	0719	52474.94	880	0.57 ^{+0.03} _{-0.04}	4.49 ^{+0.11} _{-0.12}	2.77 ^{+0.04} _{-0.12}	1.76 ^{+0.20} _{-0.47}	7.10 ^{+0.24} _{-0.33}	1.72 ^{+0.26} _{-0.22}	19.32 ^{+0.05} _{-0.04}	1.19
45	0721	52476.02	1312	0.53 ^{+0.04} _{-0.02}	4.53 ^{+0.12} _{-0.11}	2.48 ^{+0.02} _{-0.08}	1.408 ^{+0.30} _{-0.30}	7.10 ^{+0.33} _{-0.00}	2.41 ^{+0.25} _{-0.25}	20.75 ^{+0.28} _{-0.28}	1.17
46	0721	52476.08	1760	0.54 ^{+0.03} _{-0.03}	4.48 ^{+0.13} _{-0.13}	2.45 ^{+0.04} _{-0.07}	1.259 ^{+0.16} _{-0.22}	7.10 ^{+0.27} _{-0.00}	2.31 ^{+0.32} _{-0.42}	20.12 ^{+0.06} _{-0.17}	0.93
47	0721	52476.15	3520	0.52 ^{+0.03} _{-0.01}	4.55 ^{+0.52} _{-0.92}	2.44 ^{+0.02} _{-0.06}	1.256 ^{+0.07} _{-0.20}	7.10 ^{+0.18} _{-0.00}	2.88 ^{+0.08} _{-0.38}	19.78 ^{+0.07} _{-0.15}	0.78
48	0722	52477.23	1408	0.51 ^{+0.04} _{-0.01}	4.15 ^{+0.73} _{-0.62}	2.41 ^{+0.04} _{-0.06}	1.03 ^{+0.09} _{-0.20}	7.10 ^{+0.24} _{-0.00}	2.80 ^{+0.15} _{-0.50}	16.99 ^{+0.05} _{-0.31}	0.84
49	0722	52477.30	3536	0.52 ^{+0.03} _{-0.02}	4.64 ^{+0.44} _{-0.76}	2.40 ^{+0.04} _{-0.06}	0.94 ^{+0.11} _{-0.14}	7.15 ^{+0.21} _{-0.05}	2.74 ^{+0.26} _{-0.35}	16.35 ^{+0.05} _{-0.10}	0.86

NOTE. — Output of spectral parameters from an input model consisting of a multi-color blackbody, power-law, Laor line emission, and a smeared absorption Fe edge. $N_H = 4 \times 10^{21} \text{ cm}^{-2}$ was assumed throughout.

^aMidpoint of observation

TABLE 2. Fe Line Spectral Parameters for 4U 1543–47 – Laor Model

Obs No.	Date (mdd)	MJD ^a	Energy ^b (keV)	ρ^c (R_g)	Normalization ^d	Equivalent Width (eV)	Flux $\times 10^{-10e}$ (ergs cm ⁻² s ⁻¹)
1	0617	52442.83	6.58 ^{+0.39} _{-0.18}	3.54 ^{+396.46} _{-2.30}	0.019 ^{+0.014} _{-0.019}	129 ⁺⁹⁹ ₋₁₂₉	1.55 ^{+0.24} _{-0.26}
2	0617	52442.90	6.68 ^{+0.30} _{-0.28}	3.37 ^{+396.63} _{-2.14}	0.020 ^{+0.014} _{-0.020}	136 ⁺⁹⁷ ₋₁₃₆	1.67 ^{+0.27} _{-0.28}
3	0618	52443.26	6.44 ^{+0.53} _{-0.04}	3.70 ^{+396.30} _{-2.47}	0.024 ^{+0.019} _{-0.024}	110 ⁺⁸⁸ ₋₁₁₀	1.98 ^{+0.44} _{-0.47}
4	0619	52444.45	6.41 ^{+0.18} _{-0.01}	3.70 ^{+2.37} _{-2.47}	0.066 ^{+0.037} _{-0.023}	181 ⁺¹⁰³ ₋₆₄	5.29 ^{+0.78} _{-0.72}
5	0619	52444.52	6.40 ^{+0.16} _{-0.00}	3.54 ^{+2.00} _{-2.30}	0.071 ^{+0.013} _{-0.025}	188 ⁺³⁵ ₋₆₇	5.69 ^{+0.57} _{-0.70}
6	0620	52445.57	6.56 ^{+0.22} _{-0.16}	4.03 ^{+5.41} _{-2.80}	0.068 ^{+0.026} _{-0.028}	186 ⁺⁷² ₋₇₇	5.60 ^{+0.73} _{-0.58}
7	0620	52445.64	6.75 ^{+0.17} _{-0.25}	3.70 ^{+5.79} _{-2.47}	0.074 ^{+0.027} _{-0.028}	222 ⁺⁸¹ ₋₈₃	6.32 ^{+0.73} _{-0.79}
8	0621	52446.07	6.45 ^{+0.36} _{-0.06}	4.03 ^{+2.63} _{-2.80}	0.067 ^{+0.009} _{-0.040}	182 ⁺²⁶ ₋₁₀₈	5.52 ^{+0.68} _{-0.57}
9	0622	52447.00	6.42 ^{+0.28} _{-0.02}	4.03 ^{+5.26} _{-2.80}	0.060 ^{+0.026} _{-0.029}	165 ⁺⁷⁰ ₋₈₀	4.93 ^{+0.55} _{-0.69}
10	0623	52448.06	6.49 ^{+0.23} _{-0.09}	4.03 ^{+5.43} _{-2.80}	0.056 ^{+0.023} _{-0.013}	170 ⁺⁷¹ ₋₄₁	4.55 ^{+0.56} _{-0.66}
11	0624	52449.11	6.57 ^{+0.24} _{-0.18}	3.70 ^{+8.55} _{-2.47}	0.049 ^{+0.021} _{-0.025}	166 ⁺⁷³ ₋₈₅	4.04 ^{+0.53} _{-0.58}
12	0625	52450.25	6.40 ^{+0.23} _{-0.00}	3.70 ^{+5.61} _{-2.47}	0.038 ^{+0.022} _{-0.027}	132 ⁺⁷⁵ ₋₉₅	3.06 ^{+0.48} _{-0.44}
13	0626	52451.57	6.40 ^{+0.57} _{-0.00}	3.04 ^{+398.96} _{-1.81}	0.017 ^{+0.022} _{-0.017}	68 ⁺⁸⁸ ₋₆₈	1.37 ^{+0.39} _{-0.39}
14	0627	52452.69	6.40 ^{+0.19} _{-0.00}	1.24 ^{+398.77} _{-0.00}	0.020 ^{+0.020} _{-0.020}	81 ⁺⁸¹ ₋₈₁	1.64 ^{+0.43} _{-0.38}
15	0628	52453.50	6.78 ^{+0.26} _{-0.25}	3.04 ^{+20.65} _{-1.81}	0.036 ^{+0.015} _{-0.016}	208 ⁺⁸⁹ ₋₉₂	3.08 ^{+0.35} _{-0.36}
16	0628	52453.55	6.71 ^{+0.26} _{-0.31}	3.37 ^{+396.63} _{-2.14}	0.026 ^{+0.017} _{-0.023}	146 ⁺⁹⁴ ₋₁₂₈	2.19 ^{+0.32} _{-0.27}
17	0629	52454.60	6.72 ^{+0.25} _{-0.32}	3.04 ^{+396.96} _{-1.81}	0.023 ^{+0.015} _{-0.019}	149 ⁺⁹⁹ ₋₁₂₄	1.98 ^{+0.31} _{-0.34}
18	0630	52455.13	6.82 ^{+0.15} _{-0.42}	3.70 ^{+396.30} _{-2.47}	0.022 ^{+0.013} _{-0.020}	183 ⁺¹⁰⁹ ₋₁₆₇	1.93 ^{+0.21} _{-0.19}
19	0701	52456.77	6.75 ^{+0.22} _{-0.35}	3.37 ^{+396.63} _{-2.14}	0.018 ^{+0.011} _{-0.014}	173 ⁺¹⁰⁵ ₋₁₃₀	1.57 ^{+0.23} _{-0.22}
20	0702	52457.83	6.78 ^{+0.18} _{-0.33}	3.04 ^{+8.34} _{-1.81}	0.031 ^{+0.011} _{-0.014}	247 ⁺⁹¹ ₋₁₁₇	2.62 ^{+0.22} _{-0.23}
21	0703	52458.44	6.72 ^{+0.22} _{-0.32}	3.21 ^{+10.53} _{-1.97}	0.028 ^{+0.011} _{-0.015}	233 ⁺⁸⁹ ₋₁₂₁	2.40 ^{+0.27} _{-0.22}
22	0704	52459.08	6.69 ^{+0.22} _{-0.29}	3.37 ^{+12.59} _{-2.14}	0.034 ^{+0.013} _{-0.021}	229 ⁺⁸⁷ ₋₁₄₄	2.86 ^{+0.21} _{-0.30}
23	0705	52460.49	6.79 ^{+0.17} _{-0.30}	3.37 ^{+3.65} _{-2.14}	0.037 ^{+0.010} _{-0.014}	320 ⁺⁸⁵ ₋₁₁₈	3.16 ^{+0.19} _{-0.23}
24	0706	52461.41	6.76 ^{+0.21} _{-0.36}	3.04 ^{+9.07} _{-1.81}	0.028 ^{+0.011} _{-0.016}	251 ⁺¹⁰⁰ ₋₁₄₆	2.38 ^{+0.20} _{-0.20}
25	0707	52462.57	6.75 ^{+0.17} _{-0.20}	3.37 ^{+2.88} _{-2.14}	0.024 ^{+0.006} _{-0.006}	340 ⁺⁸⁴ ₋₉₁	2.01 ^{+0.15} _{-0.17}
26	0708	52463.67	6.82 ^{+0.14} _{-0.19}	3.37 ^{+2.43} _{-2.14}	0.020 ^{+0.004} _{-0.005}	389 ⁺⁸⁴ ₋₉₅	1.71 ^{+0.09} _{-0.10}
27	0709	52464.45	6.83 ^{+0.14} _{-0.43}	3.54 ^{+26.14} _{-2.30}	0.006 ^{+0.003} _{-0.003}	245 ⁺¹⁰⁹ ₋₁₄₀	0.52 ^{+0.08} _{-0.08}
28	0710	52465.08	6.86 ^{+0.11} _{-0.33}	1.24 ^{+11.99} _{-0.00}	0.008 ^{+0.002} _{-0.004}	384 ⁺¹¹³ ₋₁₉₇	0.71 ^{+0.07} _{-0.07}
29	0711	52466.34	6.81 ^{+0.16} _{-0.20}	3.37 ^{+1.68} _{-2.14}	0.008 ^{+0.002} _{-0.002}	398 ⁺⁹⁵ ₋₁₀₀	0.68 ^{+0.05} _{-0.06}
30	0712	52467.20	6.67 ^{+0.30} _{-0.27}	3.70 ^{+396.30} _{-2.47}	0.005 ^{+0.003} _{-0.005}	232 ⁺¹⁷⁷ ₋₂₃₂	0.38 ^{+0.06} _{-0.08}
31	0713	52468.66	6.89 ^{+0.08} _{-0.31}	3.37 ^{+4.03} _{-2.14}	0.005 ^{+0.001} _{-0.002}	468 ⁺¹¹² ₋₂₀₂	0.42 ^{+0.03} _{-0.05}
32	0713	52468.73	6.61 ^{+0.30} _{-0.21}	3.21 ^{+21.06} _{-1.97}	0.004 ^{+0.002} _{-0.002}	277 ⁺¹³⁶ ₋₁₇₉	0.30 ^{+0.05} _{-0.04}
33	0714	52469.24	6.85 ^{+0.12} _{-0.24}	3.04 ^{+7.25} _{-1.81}	0.005 ^{+0.001} _{-0.002}	508 ⁺¹³⁴ ₋₂₀₆	0.42 ^{+0.04} _{-0.05}
34	0714	52469.31	6.67 ^{+0.19} _{-0.27}	3.37 ^{+10.48} _{-2.14}	0.004 ^{+0.001} _{-0.002}	395 ⁺¹²¹ ₋₂₀₀	0.37 ^{+0.04} _{-0.03}
35	0715	52470.24	6.59 ^{+0.38} _{-0.19}	3.37 ^{+396.63} _{-2.14}	0.004 ^{+0.001} _{-0.004}	363 ⁺¹⁴¹ ₋₃₆₃	0.31 ^{+0.05} _{-0.05}
36	0715	52470.30	6.40 ^{+0.20} _{-0.00}	1.24 ^{+20.20} _{-0.00}	0.002 ^{+0.002} _{-0.002}	153 ⁺¹²⁰ ₋₁₄₉	0.16 ^{+0.08} _{-0.04}
37	0716	52470.98	6.40 ^{+0.57} _{-0.00}	3.87 ^{+396.13} _{-2.63}	0.001 ^{+0.002} _{-0.001}	125 ⁺²¹⁸ ₋₁₂₅	0.09 ^{+0.08} _{-0.07}
38	0716	52471.02	6.84 ^{+0.13} _{-0.44}	1.24 ^{+398.77} _{-0.00}	0.001 ^{+0.002} _{-0.001}	153 ⁺³¹⁹ ₋₁₅₃	0.09 ^{+0.05} _{-0.05}
39	0717	52472.62	6.40 ^{+0.27} _{-0.00}	3.38 ^{+10.53} _{-2.14}	0.002 ^{+0.002} _{-0.001}	227 ⁺²⁹² ₋₁₇₉	0.14 ^{+0.04} _{-0.04}
40	0717	52472.69	6.56 ^{+0.41} _{-0.16}	3.70 ^{+42.04} _{-2.47}	0.002 ^{+0.002} _{-0.002}	274 ⁺²²⁴ ₋₂₇₄	0.16 ^{+0.04} _{-0.04}
41	0718	52473.20	6.57 ^{+0.14} _{-0.17}	3.37 ^{+12.63} _{-2.14}	0.002 ^{+0.002} _{-0.001}	227 ⁺¹⁸¹ ₋₁₁₂	0.16 ^{+0.04} _{-0.04}
42	0718	52473.27	6.40 ^{+0.31} _{-0.00}	1.24 ^{+37.22} _{-0.00}	0.002 ^{+0.001} _{-0.002}	202 ⁺¹⁵⁶ ₋₁₇₈	0.14 ^{+0.03} _{-0.04}
43	0719	52474.18	6.40 ^{+0.20} _{-0.00}	3.37 ^{+2.38} _{-2.14}	0.003 ^{+0.002} _{-0.002}	313 ⁺²⁰³ ₋₂₁₀	0.28 ^{+0.06} _{-0.05}
44	0720	52474.94	6.89 ^{+0.08} _{-0.24}	3.04 ^{+1.72} _{-1.81}	0.004 ^{+0.003} _{-0.001}	442 ⁺²⁹³ ₋₁₃₇	0.36 ^{+0.04} _{-0.05}
45	0721	52476.02	6.40 ^{+0.12} _{-0.00}	3.04 ^{+1.63} _{-1.81}	0.004 ^{+0.003} _{-0.001}	289 ⁺¹⁹⁹ ₋₄₇	0.36 ^{+0.05} _{-0.05}
46	0721	52476.08	6.43 ^{+0.17} _{-0.04}	3.04 ^{+3.19} _{-1.81}	0.005 ^{+0.002} _{-0.002}	332 ⁺¹⁶² ₋₁₂₇	0.38 ^{+0.04} _{-0.06}
47	0721	52476.15	6.40 ^{+0.15} _{-0.00}	1.40 ^{+4.65} _{-0.16}	0.003 ^{+0.001} _{-0.001}	194 ⁺⁷⁶ ₋₆₃	0.23 ^{+0.04} _{-0.04}
48	0722	52477.23	6.40 ^{+0.10} _{-0.00}	3.04 ^{+2.15} _{-1.81}	0.003 ^{+0.003} _{-0.001}	228 ⁺²⁰³ ₋₈₂	0.23 ^{+0.06} _{-0.04}
49	0722	52477.30	6.40 ^{+0.10} _{-0.00}	3.04 ^{+1.69} _{-1.81}	0.003 ^{+0.002} _{-0.001}	281 ⁺¹⁵⁹ ₋₁₁₁	0.27 ^{+0.03} _{-0.03}

NOTE. — Output of spectral parameters from an input model consisting of a multi-color blackbody, power-law, Laor line emission, and a smeared absorption Fe edge. $N_H = 4 \times 10^{21}$ cm⁻² was assumed throughout.

^aMidpoint of observation.

^b'Laor' model in XSPEC with the following fixed parameters: power-law=3, $i=21^\circ$, $R_{out}=400R_g$ ($R_g = GM/c^2$).

^cInner radius in units of R_g .

^dPhotons cm⁻² s⁻¹ in the line.

^eUnabsorbed flux in the 3–25 keV band.

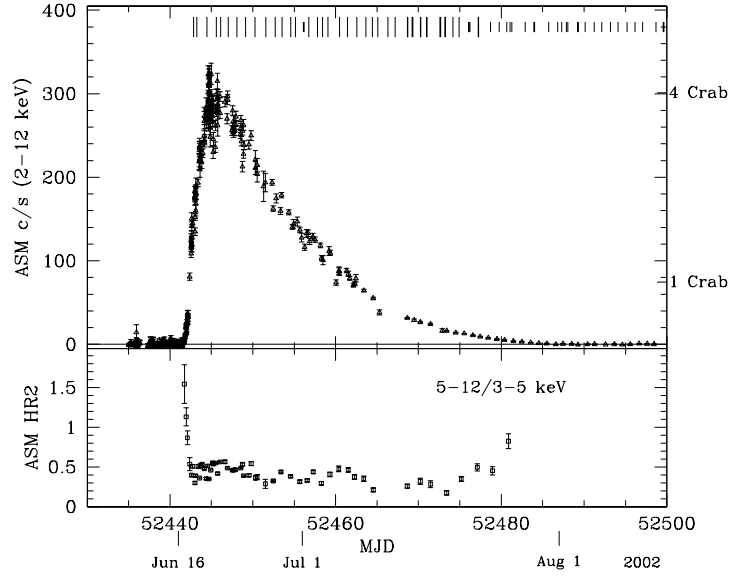


FIG. 1.— (Upper Panel) 2–12 keV ASM light curve and (Lower Panel) hardness ratio (5–12 keV)/(3–5 keV) for 4U 1543–47. The vertical lines at the top indicate the times of pointed RXTE observations; the larger tickmarks indicate observations analyzed in this paper.

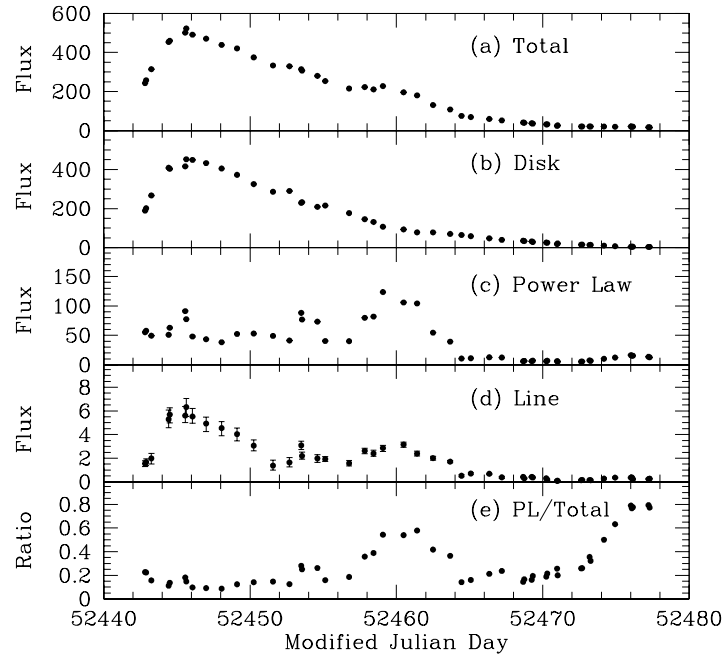


FIG. 2.— (a) Total flux, (b) disk flux, (c) power-law flux, (d) line flux, and (e) ratio of the power-law flux to the total flux for PCA observations of 4U 1543–47 in the 3–25 keV band. All fluxes are given in units of 10^{-10} ergs cm^{-2} s^{-1} . When error bars are not visible, it is because they are smaller than the plotting symbol.

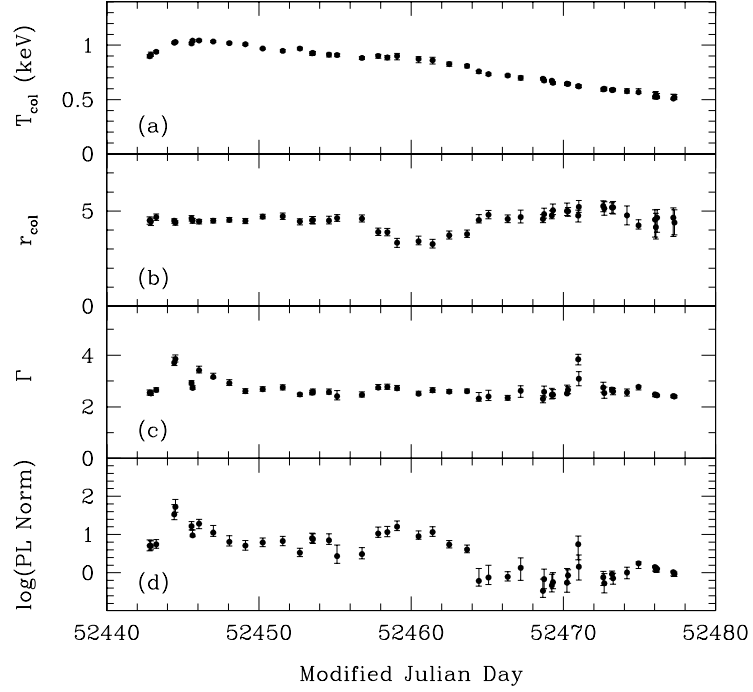


FIG. 3.— Spectral parameters for PCA observations of 4U 1543–47. The plot shows (a) the temperature at the inner disk radius in keV, (b) the inner disk radius in units of gravitational radii, (c) the power-law photon index Γ , and (d) the power-law normalization in units of photons $\text{keV}^{-1} \text{cm}^{-2} \text{s}^{-1}$ at 1 keV, plotted on a semi-log scale. When error bars are not visible, it is because they are smaller than the plotting symbol.

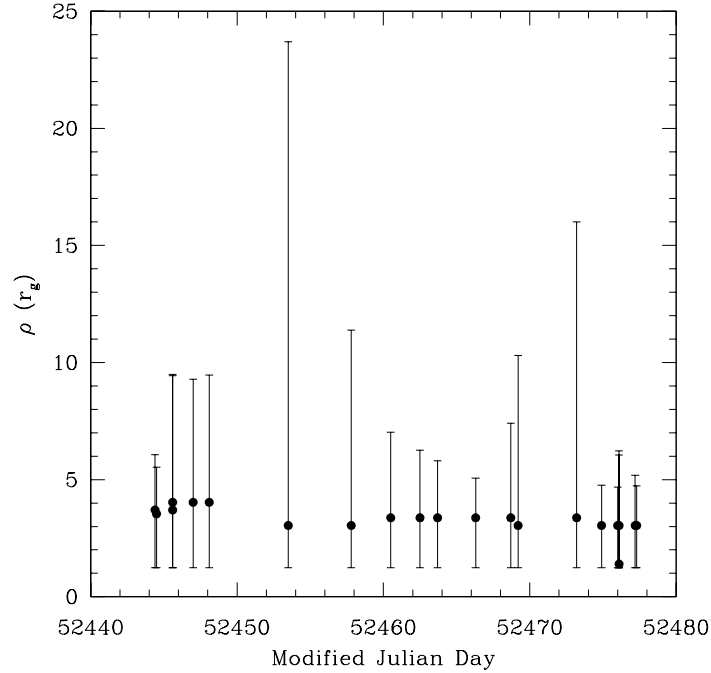


FIG. 4.— Evolution of ρ . The inner disk radius in units of gravitational radii as measured by the Laor line model is plotted against time. Only those observations for which the equivalent width is greater than two times the minus side error in equivalent width are plotted. The error bars are systematically large due to the poor resolution of *RXTE*, though the data points appear relatively stable. The lower bound on each error bar is $\rho = 1.235$ because that is the radius of the innermost stable circular orbit for a prograde black hole with dimensionless angular momentum $a_* = 0.998$ (Thorne 1974).

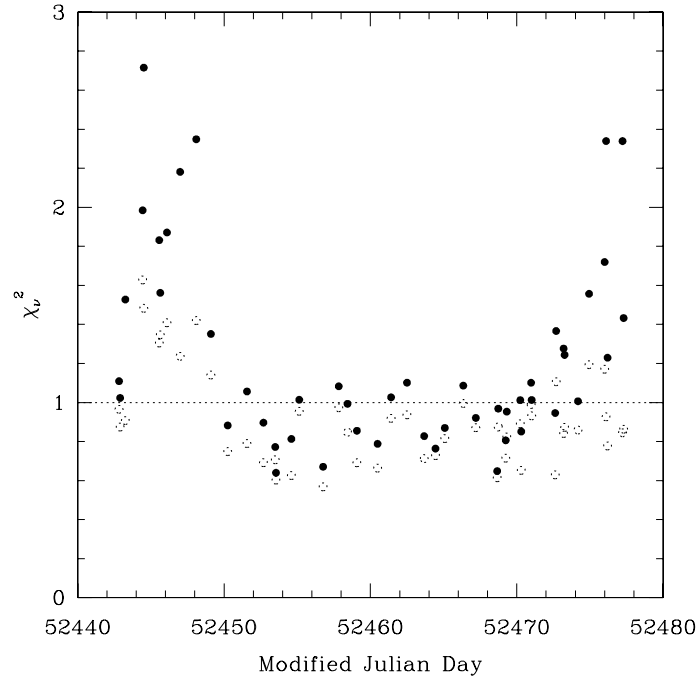


FIG. 5.— Comparison between the Laor model and the Gaussian model for a fit of the Fe line component. The solid circles show the χ^2_ν values for the Gaussian model. The open circles show the χ^2_ν values for the Laor model. Both models also include interstellar absorption, disk blackbody, power-law, and smeared edge components.

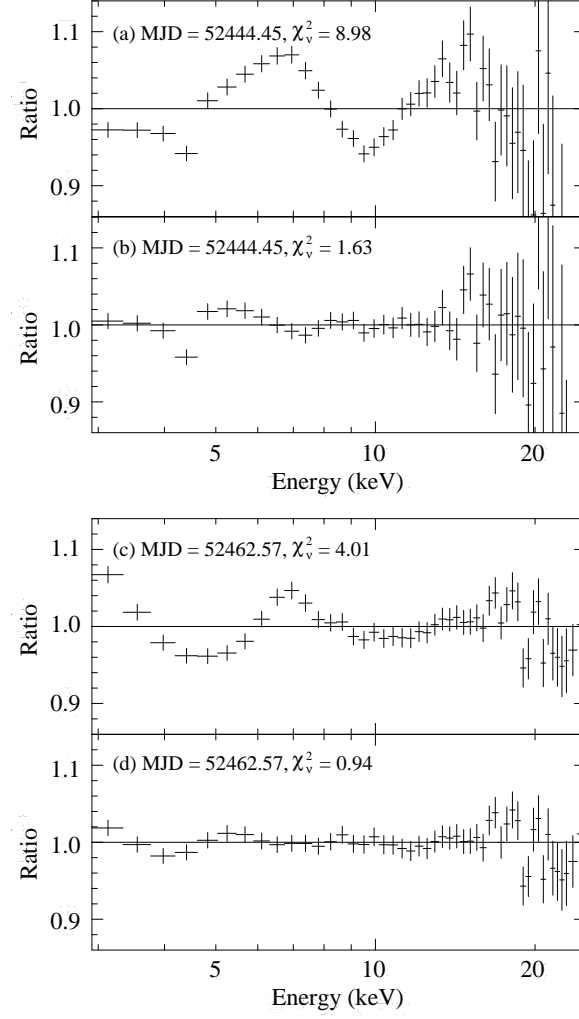


FIG. 6.— Sample PCA residuals. Note in (a) the appearance of a strong, asymmetric Fe $K\alpha$ line. Plots (a) and (c) show fits to a model consisting of a multi-color disk blackbody, power-law, and an interstellar absorption fixed at $N_H = 4 \times 10^{21} \text{ cm}^{-2}$. Plots (b) and (d) show the fits after the inclusion of the Laor model and a smeared absorption edge.

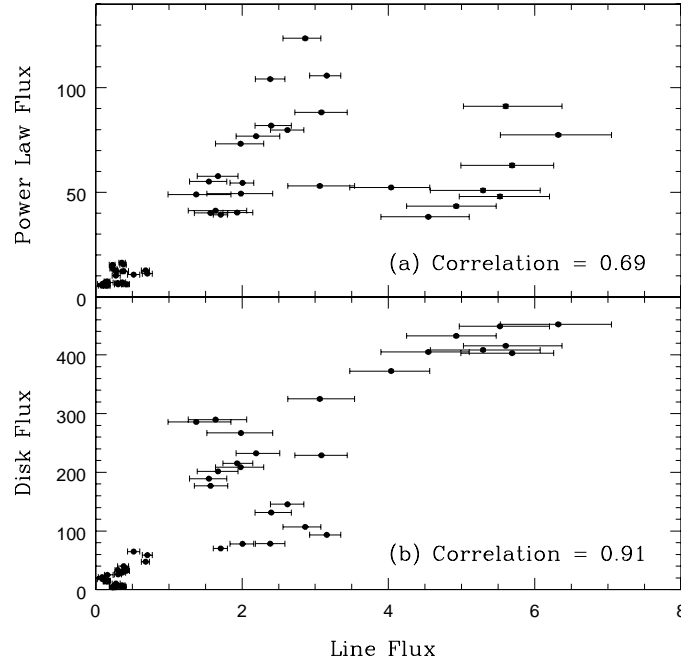


FIG. 7.— Correlations between line flux and other flux parameters. All fluxes given in units of 10^{-10} ergs cm^{-2} s^{-1} . The correlation coefficients were calculated using the linear Pearson correlation test. Errors are plotted for both the vertical and horizontal directions. When error bars are not visible, it is because they are smaller than the plotting symbol.

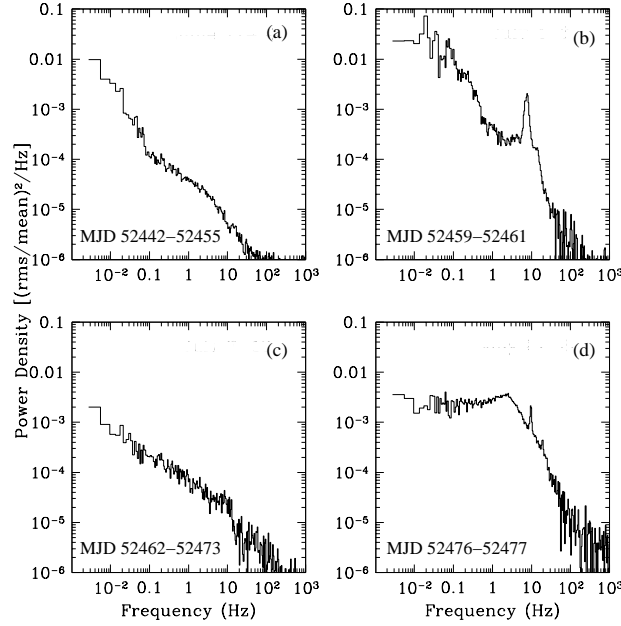


FIG. 8.— Average power density spectra for 4U 1543–47. PDS taken in the frequency range 4 mHz–4 kHz for data within 2–30 keV during four time intervals of the observation. The gaps in the time intervals represent days when the source is in transition. Note the presence of a strong QPO in panel (b).

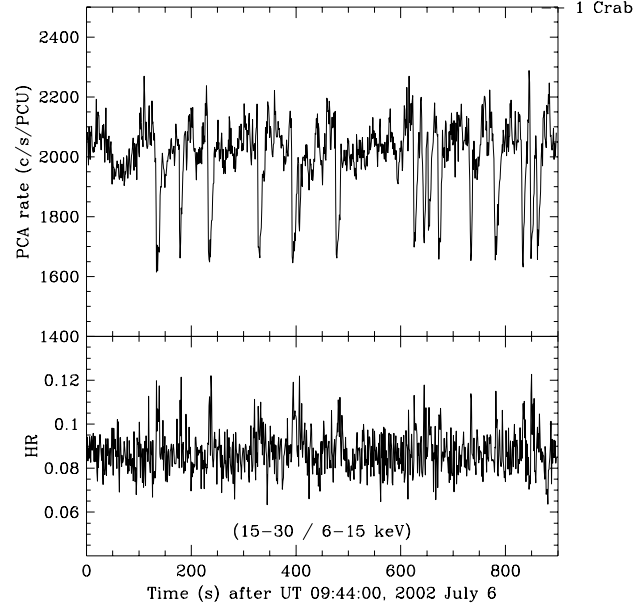


FIG. 9.— Light curve of 4U 1543–47 on MJD 52461. The top panel shows the light curve with hard dips suggestive of an accretion instability. The dips last 5–10 s, with a dip rate of roughly one per minute. The PCA hardness ratio is plotted in the bottom panel.

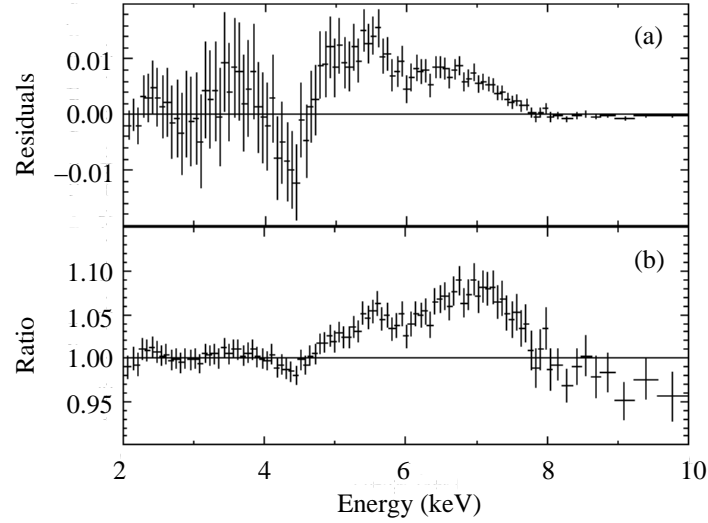


FIG. 10.— Data from *EXOSAT*/GSPC taken in 1983 (see van der Woerd et al. 1989). The continuum is fit to a disk blackbody and power-law model, and includes interstellar absorption. The line is fit to a Laor profile. Panel (a) show the residuals in units of normalized counts $\text{sec}^{-1} \text{keV}^{-1}$. Panel (b) shows the ratio of the data to the model. Note the clear double-peaked structure of the line profile.